Strain partitioning and damage initiation in a continuously cooled carbide free bainitic steel

Hajizad, O.; Kumar, A.; Petrov, R. H.; Sietsma, J.; Dollevoet, R.; Li, Z.

DOI
10.1016/j.commatsci.2021.110965

Publication date
2022

Document Version
Final published version

Published in
Computational Materials Science

Computational Materials Science 202 (2022) 110965

Contents lists available at ScienceDirect

Computational Materials Science

journal homepage: www.elsevier.com/locate/commatsci

Strain partitioning and damage initiation in a continuously cooled carbide free bainitic steel

O. Hajizad [a], A. Kumar [b], R.H. Petrov [b,c], J. Sietsma [b,c], R. Dollevoet [a], Z. Li [a,*]

[a] Section of Railway Engineering, Faculty of Civil Engineering and Geoscience, Delft University of Technology, Delft, the Netherlands
[b] Department of Materials Science and Engineering, Delft University of Technology, Delft, the Netherlands
[c] Department of Electrical Energy, Metals, Mechanical Constructions & Systems, Ghent University, Ghent, Belgium

ARTICLE INFO

Keywords:
Carbide free bainitic steel
Damage initiation
Microstructural modeling
Crystal plasticity finite element method (CPFEM)
Crystal plasticity fast Fourier transform (CPFFT)

ABSTRACT

Microscopic stress and strain partitioning control the mechanical and damage behavior of multiphase steels. Using a combined numerical and experimental approach, local strain distributions and deformation localization are characterized in a carbide free bainitic steel produced by continuous cooling. The microstructure of the steel consists of bainite (aggregate of bainitic ferrite and thin film retained austenite), martensite and blocky retained austenite.

Numerical simulations were done using a von Mises J2 plasticity flow rule and also a phenomenological crystal plasticity material model. The representative volume element (RVE) was created using a realistic 2D geometry captured through Electron Backscatter Diffraction (EBSD). These simulations describe the strain distribution and deformation localization in this steel. To validate the simulation results, local strain maps were obtained experimentally via *in-situ* tensile testing using micro digital image correlation (μDIC) in scanning electron microscopy (SEM). The information gained from numerical and experimental data gave valuable insight regarding the microstructural features responsible for strain partitioning and damage initiation in this carbide free bainitic steel. The results of the modelling show that martensite, martensite/bainitic ferrite interfaces, interface orientation with respect to tensile direction, bainitic ferrite size and phase composition influence the strain partitioning in this carbide free bainitic steel.

1. Introduction

Pearlitic steels are commonly used in railway applications. Due to demands of future railway transport, there is a need for better materials that can endure the high contact stresses which over time lead to rolling contact fatigue [1–3] and wear [4,5] in rails. Bainitic steels have gained a lot of attention in rail industries due to their higher strength and toughness than the pearlitic counterparts [6,7]. The conventional bainitic microstructure contains a mixture of bainitic ferrite with fine cementite (carbide) laths (or particles) in between them. The presence of cementite laths can lead to void initiation or cleavage in the bainitic microstructure and is detrimental for the fatigue life of the steel [8]. The cementite precipitation in bainitic steels can be suppressed by the addition of Si during the alloy design [9,10]. The bainitic transformation in the presence of high Si (1.3–2.0 wt%) results in a carbide free bainitic microstructure which contains bainitic ferrite, retained austenite and martensite. The retained austenite usually exists in two morphologies: *(i)* thin film retained austenite (TFRA) between bainitic ferrite *(ii)* blocky retained austenite (BRA), which is distributed between bainitic regions [8]. The TFRA acts against crack propagation [8] and the aggregate it produces together with fine bainitic ferrite results in high strength, toughness and hardness [11–13]. These steels also offer better rolling contact fatigue (RCF) characteristics compared to conventional pearlitic steels [14,15]. Therefore, carbide free bainitic steels could be a good candidate for railway applications.

Heterogeneous deformation in metals can initiate damage. Proper modelling of this heterogeneous deformation would result in prediction of locations where cracks form. The knowledge about these damage initiation sites would help to design stronger and more damage resistant metals. Many researchers have studied such heterogeneous deformation and damage in metals [16–26].

The crystal plasticity (CP) has been successfully used to describe the

* Corresponding author at: Delft University of Technology, Faculty of Civil Engineering and Geosciences, building 23, Stevinweg 1, 2628 CN, Delft, the Netherlands.
E-mail address: z.li@tudelft.nl (Z. Li).

https://doi.org/10.1016/j.commatsci.2021.110965
Received 23 July 2021; Received in revised form 7 October 2021; Accepted 8 October 2021
Available online 23 October 2021

anisotropic deformation modes of metallic materials (such as dislocation slip and deformation twining). This methods can effectively describe the micromechanical behavior of polycrystalline materials and has been used by many researchers to simulate the damage accumulation and fracture [27–35].

The mechanical response and damage behavior in multi-phase complex steels are governed by microscopic strain and stress partitioning among the microstructural constituents. Such complex microstruture with different phases would produce highly non-uniform partitioning of stresses and strains in the microstructure. The stress/strain partitioning can lead to severe deformation localization and eventually can initiate damage during the application of mechanical loading [36,37]. However, the complexity of the microstructure makes it difficult to capture such strain partitioning and damage response. Many numerical and experimental studies have been performed on dual phase steels and some of these studies have combined both numerical and experimental methods in order to study the damage mechanism [37–50]. But there exist only few studies on the damage and strain partitioning phenomena in the complex bainitic microstructures [35,51] such as Continuously Cooled Carbide Free Bainitic Steels (CC-CFBS) (industrially known as B360). Therefore, a detailed investigation is needed to study the local deformation and microscopic damage mechanisms in these steels, in relation to their microstructural constituents.

Numerical models have been established to study the material micromechanical behavior using a simplified geometry based on the Voronoi algorithm [43,52]. Recently, development of computational tools has enabled to investigate the material response by considering its realistic microstructure [33,35,40,41,44,51,53–56]. Many researchers [36,57–61] have performed *in-situ* experiments with micro Digital Image Correlation (μDIC) to measure local strain maps in steels. Such experiments are useful for the validation of numerical models. However, few studies have been performed using a combined numerical and experimental approach on the same geometry so that the local strain maps obtained from simulations could be validated using *in-situ* experiment [62–64].

In this research, we use this combined approach where numerical simulations are validated using the *in-situ* experimental results, on the microstructure of a CC-CFBS. Both the simulations and the experiment were performed on the same microstructure. Using this approach, the strain partitioning and damage initiation behavior of this CC-CFBS has been investigated. Numerical simulations using two different methods including: *(i)* a von Mises J2 plasticity model within the framework of continuum mechanics (via Abaqus) and *(ii)* a phenomenological crystal plasticity finite element approach (via DAMASK, the Düsseldorf Advanced Material Simulation Kit, [65]) using a fast Fourier solver [66], have been performed. The representative volume element (RVE) for the numerical models has been created using 2-dimensional microstructure of CC-CFBS, obtained through Electron Backscatter Diffraction (EBSD). The validation was done via *in-situ* tensile experiment with μDIC in Scanning Electron Microscope (SEM) in combination with EBSD.

The combined numerical and experimental investigation on the damage mechanisms in CC-CFBS provides valuable insight into damage initiating microstructural factors. This would help to optimize the microstructure by removing/reducing these factors, which would result in steels with better mechanical performance such as high strength and toughness.

2. Methodology

2.1. Material

The chemical composition of continuously cooled carbide free bainitic steel (B360) is verified by a combined use of Optical Emission Spectrometry (OES) and X-ray Fluorescence Spectrometry (XRF) techniques and is presented in Table 1. The final microstructure is produced by continuous cooling in the air from fully austenitic temperature range.

Table 1
Chemical composition of B360 (in wt.%).

Steel Grade	C	Cr	Mn	Si	V	Mo
B360	0.27	0.51	1.55	1.36	0.03	0.15

Low carbon content is selected in the current alloy in order to have good weldability and fast bainitic transformation kinetics [67]. By using silicon, carbide formation is suppressed and carbide-free bainitic microstructure is obtained [9,10].

2.1.1. EBSD analysis

The EBSD characterization was performed by an FEI Quanta-450 SEM with a field emission gun (FEG). To collect EBSD data, a Hikari-Pro EBSD detector together with an EDAX-TSL OIM Data Collection software was utilized. Accelerating voltage was 15 kV and a step size of 50 nm was employed in a hexagonal scan grid mode for all scans. To analyze the EBSD data a TSL OIM data analysis v. 7.0 software was used. The points with a confidence index$<$0.1 were excluded from quantification.

The EBSD analysis of this steel is presented in Fig. 1. Fig. 1(a) shows the phase map of B360. Bainite, which is a lamellar structure of bainitic ferrite [68], is shown in red and (blocky) retained austenite in green. However, the EBSD phase map can not distinguish between bainite and martensite and they are both represented in red. It is possible to separate martensite from bainite using image quality (IQ) maps. Martensitic islands have lower IQ than the bainitic ferrite, which is due to high dislocation density that reduces the quality of the diffraction pattern [69,70]. The lower IQ values mean that martensite in the microstructure would appear darker in IQ maps. Fig. 1(b) shows the phase map together with the IQ map while Fig. 1(c) shows the martensite distribution, represented in black. The EBSD analysis shows that B360 steel consists of about 64% bainite, about 22% M, and around 14% retained austenite.

2.1.2. SEM analysis

Analyses of the SEM images were conduced in order to measure some microstructural characteristics that will be discussed at Section 2.2.2. The SEM was performed on a JEOL JSM-IT100 microscope with a tungsten filament. The accelerating voltage was 10 kV and working distance was 6.6 mm.

2.2. Numerical models

In order to simulate the strain partitioning and damage behavior of the B360 under tensile loading, a von Mises J2 plasticity finite element model (VPFEM) and a phenomenological crystal plasticity model using a fast Fourier transform solver (CPFFT) [65,66] were applied. For the former, Abaqus software and for the latter the framework of DAMASK [44] are used. DAMASK provides various constitutive models, of which phenomenological power law (a dislocation-based model) [46,47] is applied in this research. The flow curves of individual phases are calculated by using a dislocation-density-based strain hardening model (section 2.2.2.) and later used to calibrate these material models.

2.2.1. Representative volume element

Representative volume element (RVE) approach [71] was employed to create a representative geometry from the actual microstructure of the B360 steel. The RVE model represents phase distribution and morphology, shape, size and spatial distribution of the different phases. Using the EBSD data a 2D RVE was built from the actual microstructure of B360 (Fig. 1).

Based on another study on the exact same grade, we know that most of retained austenite transforms into martensite during *in-situ* tensile testing in a deformation induced martensitic transformation mechanism [72]. This study shows that large BRA islands (with grain size $>$ 0.25 μm) are less stable compared to finer or nano-crystalline retained

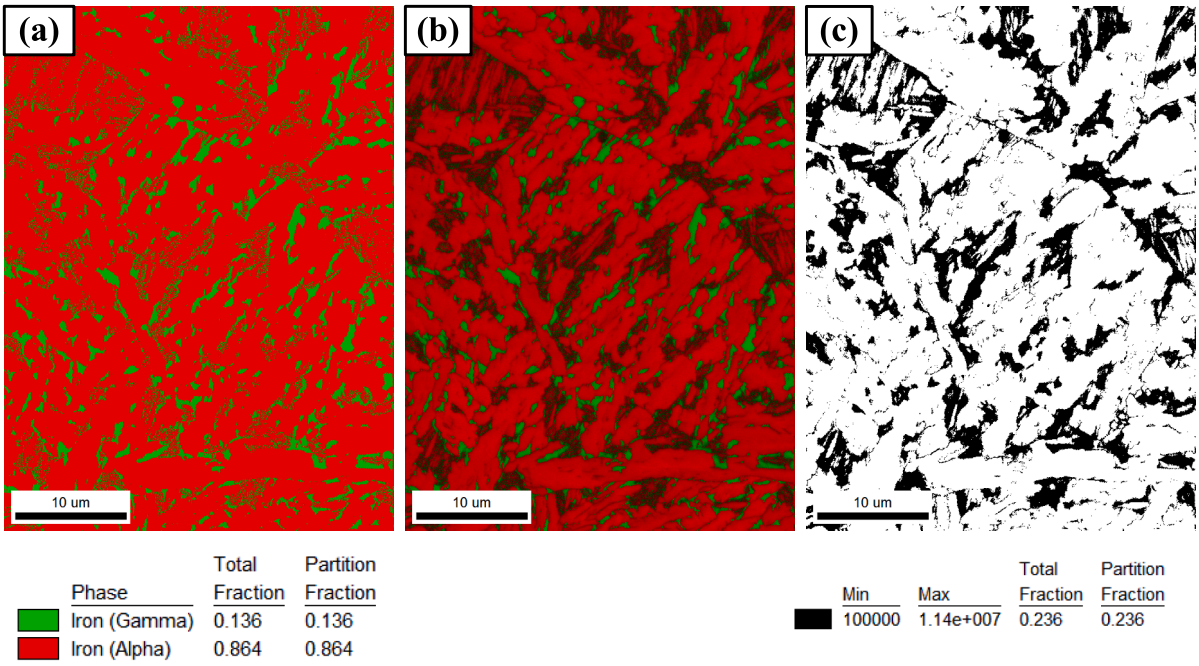

Fig. 1. EBSD map of B360, (a) phase distribution map, (b) IQ and phase fraction map, (c) the IQ map, showing martensite distribution (as dark areas).

austenite islands during mechanical deformation. Based on this information and for simplicity, it is assumed that all of BRA tranforms into martensite at the beginning of straining. So, the microstructure will be consisting of a bainite costituent and a martensite phase. In the bainite, which is an aggregate of TFRA and bainitic ferrite, the TFRA cannot be indexed in the EBSD due to the limit of spatial resolution and hence the aggregate of bainitic ferrite and TFRA is considered as one homogeneous microstructural constituent in the numerical model, named as bainite. The resulting RVE is shown in Fig. 2(a). The EBSD data is then edited using MATLAB based codes [73] and cleaned from the pixels which are non-indexed, have low confidence index (CI) and belong to unreasonably small grains. These pixels are filled with phase ID, grain ID and orientations equal to those of the grain that surrounds these removed pixels. In order to prepare the input for the VPFEM, this edited EBSD data set is meshed and prepared for Abaqus as shown in Fig. 2(b).

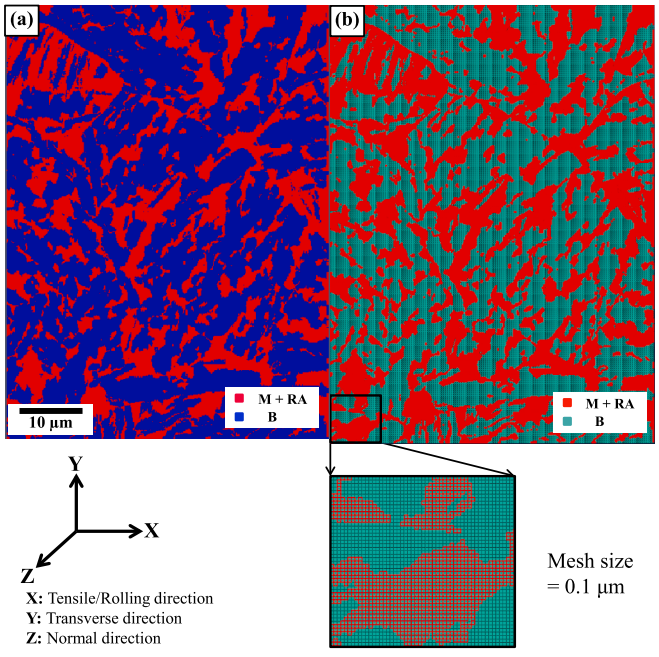

Fig. 2. Selection of the RVE from the EBSD and creating the geometry input for models, (a) The RVE input into spectral solver of DAMASK, (b) The RVE input into Abaqus after meshing.

However, for DAMASK there is no need of meshing and the input data (geometry, material texture and phase distribution) can be extracted from the same edited EBSD data set, using the tools already implemented in DAMASK.

2.2.2. *Mechanical properties of each phase*

There have been several studies to measure the mechanical properties of each phase in steels [40,41,74]. In this work, all phases were assumed to be homogeneous. The flow curve of the individual constituents of martensite and bainite is estimated using a dislocation-based strain hardening model [74] which originates from classical dislocation theory [75–77]. The nano-hardness test has shown that this model has a good estimation of the stress–strain relation of the single phases [74]. The elastic properties of B360 steel was calculated in [68] as $E =$ 202.6 MPa and $\upsilon = 0.3$, with E the Young's modulus and υ the poisson ratio.

The stress–strain relation is presented as follows [74]:

$$\sigma = \sigma_0 + \Delta\sigma + \alpha M \mu \sqrt{b} \sqrt{\frac{1 - \exp(-M.k.\varepsilon)}{kL}} \tag{1}$$

where σ is flow stress (von Mises). The first term (σ_0) takes care of the dislocation strengthening effect as well as work softening due to recovery. Second term ($\Delta\sigma$) is the additional strengthening due to the precipitation or the carbon in solution and the last term is the strain-dependent part where ε is the true plastic strain (equivalent plastic strain).

The value of σ_0 which is called the Peierls stress is calculated using the effects of alloying elements in the solid solution.

$$\sigma_0 = 77 + 80 \times (\%\mathrm{Mn}) + 750 \times (\%\mathrm{P}) + 60 \times (\%\mathrm{Si}) + 80 \times (\%\mathrm{Cu}) + 45 \times (\%\mathrm{Ni}) + 60 \times (\%\mathrm{Cr}) + 11 \times (\%\mathrm{Mo}) + 5000 \times (\%\mathrm{N_{ss}}) \tag{2}$$

The fraction of alloying elements in bainite and martensite is taken the same as the bainitic B360 steel which is presented in Table 1.

However, the carbon content is different in the two constituents. The

carbon content of bainitic ferrite is taken to be 0.1% [78,79] and in martensite 0.58%.

For bainite, the effect of dislocation strengthening is strong and more influential than the solid solution carbon strengthening effect [81]. $\Delta\sigma$ for bainite is dependent on prior austenite grain size (PAGS) and transformation temperature [80,82]. Low bainitic transformation temperature would result in high density of transformation dislocations and higher $\Delta\sigma$ value as well. PAGS indirectly influences the $\Delta\sigma$ value since it can influence bainitic transformation temperature and kinetics [80–82]. Since the $\Delta\sigma$ for bainite cannot be determined directly, we have used the same approach as in [83] and the same rule of mixtures is used to calculate the value of $\Delta\sigma_b$ for bainite. The hardness of B360 steel, which was measured as 344 HV0.1 is equal to the hardness of DP1000 dual phase steel, which contains 0.15% carbon [84] with 48% ferrite and 52% martensite volume fraction.

For martensite and ferrite $\Delta\sigma$ is calculated as follows [80]:

$$\Delta\sigma_m = 3065\left(\%C_{ss}^{m}\right) - 161 \tag{3}$$

$$\Delta\sigma_f = 5000(\%C_{ss}^{f}) \tag{4}$$

where C_{ss}^{m} is carbon content (wt%) in martensite and C_{ss}^{f} is carbon content (wt%) in ferrite.

And $\Delta\sigma_b$ can be measured as follows:

$$\Delta\sigma_b = \Delta\sigma_f \times V_f + \Delta\sigma_m \times V_m \tag{5}$$

where V_f and V_m are the volume fraction of ferrite and martensite (in DP1000 steel), respectively. Using this approach, the value of $\Delta\sigma_b$ was calculated to be 365 MPa.

The last term in Eq. (1) considers the strain dependency. The constant α is equal to 0.33, M is Taylor factor ($M = 2.75$) [51], μ is the value of shear modulus ($\mu = 77.9$ GPa) and b is the length of Burger vector ($b = 2.5 \times 10^{-10}$ m). The dislocation mean free path L for ferrite, is considered equal to the average grain diameter (d_α), for martensite, it is 3.8×10^{-8} m [74,85] and for bainite is assumed to be the average distance between low angle grain boundaries [83]. The average bainitic lath width was calculated as 0.55 ± 0.09 μm by using the SEM images captured from various bainitic laths, for which two of these cases are shown in Fig. 3. So, the L for bainitic ferrite is measured to be 0.55 μm.

The recovery rate k is $10^{-5}/d_\alpha$ for ferrite, and 41 for martensite [82,83,86]. For bainite, k is considered to be $10^{-5}/d_\gamma$, where d_γ is the PAGS [83,87].

Fig. 4(a) represents the EBSD phase map (red color showing Iron-Alpha and green color showing Iron-Gamma phase) overlapped with IQ for the original RVE. Fig. 4(b) shows the inverse pole figure (IPF) map overlapped with IQ map of the considered RVE. Since the size of this RVE was small compared to the prior austenite grains (PAGs) (as shown in Fig. 4(b)) and not statistically suitable to measure the PAGS, another larger region of B360 was examined. The phase map overlapped with IQ map of this second region is shown in Fig. 4(c) and its IPF map is shown in Fig. 4(d). All IPF maps are plotted in the normal direction. In order to calculate the PAGS of the second region of B360, the PAGs were reconstructed from the EBSD maps, using ARPGE 2.4 software [88]. We considered Nishiyama-Wassermann (N-W) orientation relationships for this reconstruction. The PAGs were further plotted using TSL OIM Analysis v. 7.0 software and shown in Fig. 4(e). The average PAGS was calculated (using the second region data) as 26 ± 9 μm. From this measurement the k was calculated for bainite.

Based on these measurements and calculations, the stress–strain curves for bainite and martensite are plotted in Fig. 5.

2.2.3. von Mises J2 plasticity material model

In this model, for both phases von Mises J2 plasticity material model with an isotropic hardening law is used. The flow behavior shown in Fig. 5 is used and yield stress is given as a function of plastic strain. The RVE mentioned in section 2.2.1. is used with a mesh size of 0.1 μm. Periodic boundary conditions (PBC) are applied using a python-based code to impose the repetitive deformation on this RVE. In order to do so the meshing should be in a way that nodes on opposite sides of the RVE are equal in number and space.

PBCs [89] imply that the macroscopic geometry of the bigger model can be constructed by spatially repeating the RVE. Using such boundary conditions also results in periodic deformation of the micromechanical model. These boundary conditions are defined as follows [90] and shown in Fig. 6:

$$\vec{x}_R = \vec{x}_L + \vec{x}_2 - \vec{x}_1, \tag{6}$$

$$\vec{x}_T = \vec{x}_B + \vec{x}_4 - \vec{x}_1, \tag{7}$$

where $\vec{x}_R, \vec{x}_L, \vec{x}_B$ and $\vec{x}_T$ are a position vector on the right, left, bottom and top of the boundary of RVE. And $\vec{x}_i, i = 1, 2, 4,$ are the position vectors of the corner points 1, 2 and 4 (in deformed state).

Other proper boundary conditions were also imposed to remove rigid body motion and apply uniaxial tensile displacement. Then simulation was performed and the strain localization results were postprocessed which will be discussed in section 3.

2.2.4. Phenomenological crystal plasticity material model

The geometry definition for the CPFFT model is done using the EBSD

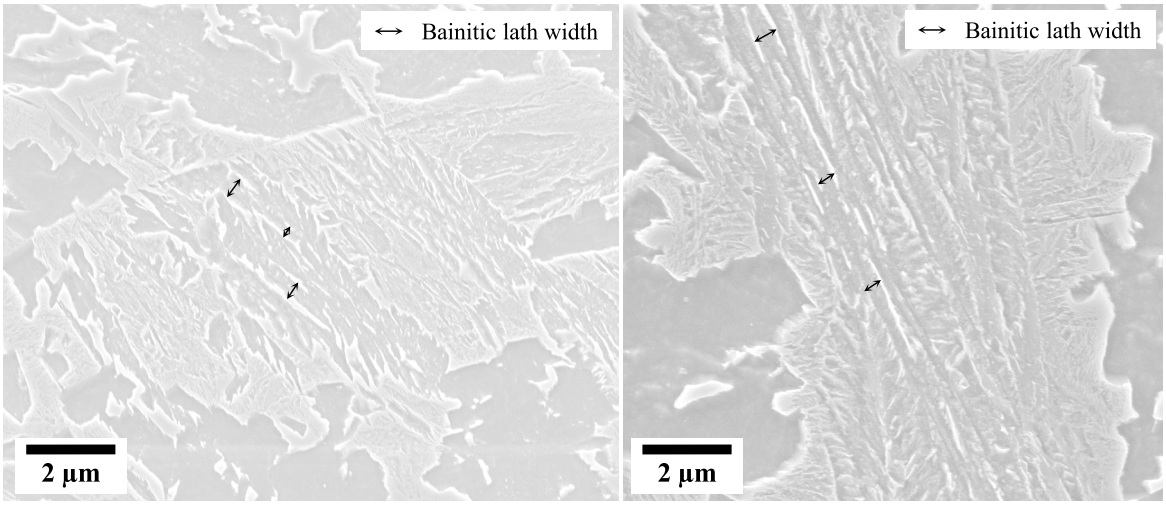

Fig. 3. SEM images from different bainitic laths.

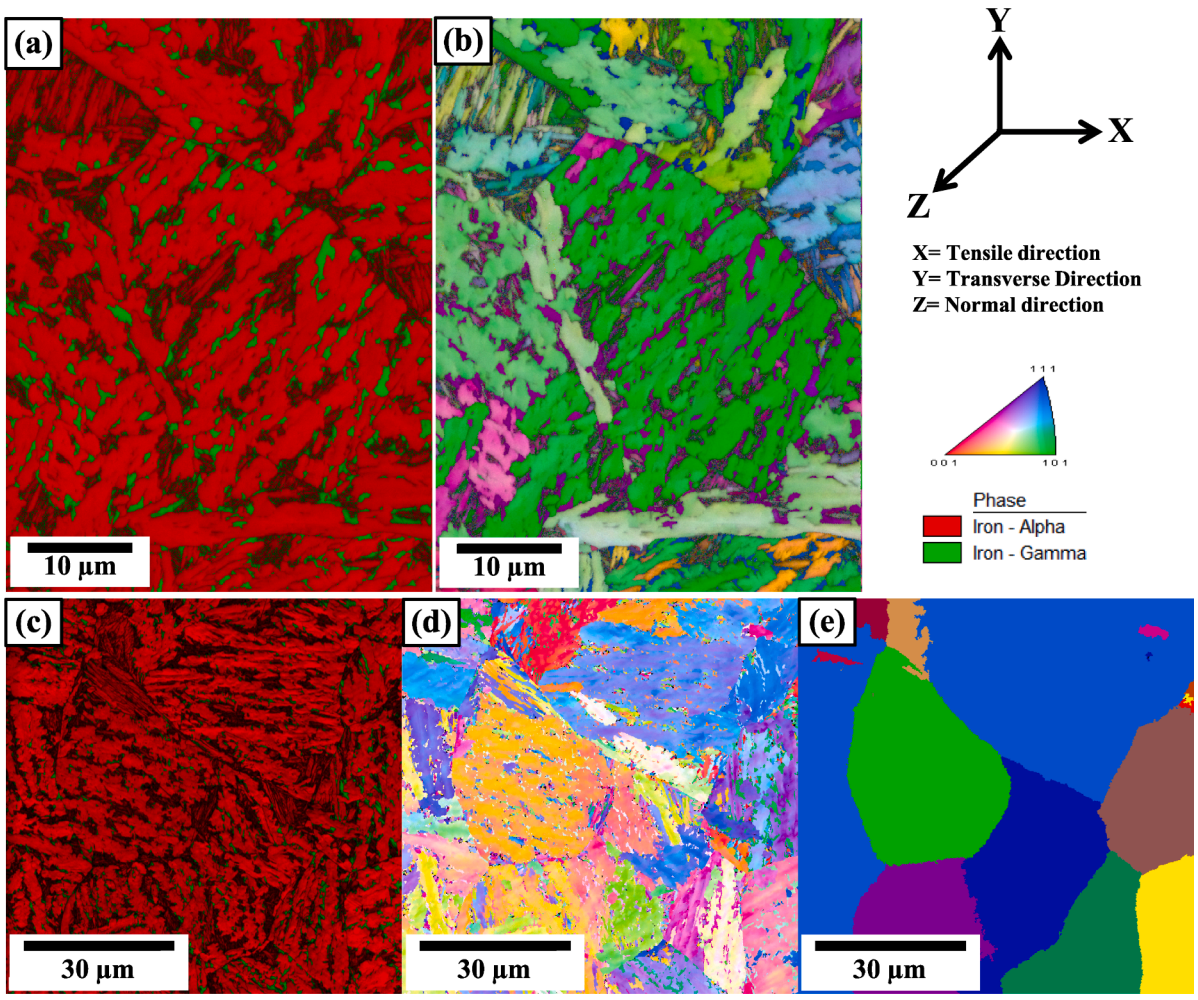

Fig. 4. EBSD maps of two different regions of B360, (a) The phase map overlapped with IQ map of the considered RVE created from first region, (b) IPF map overlapped with IQ map of the considered RVE, (c) The phase map overlapped with IQ map of second region of B360, (d) IPF map of second region of B360 (IPFs are plotted in the normal direction), (e) Grain map of the reconstructed PAGs.

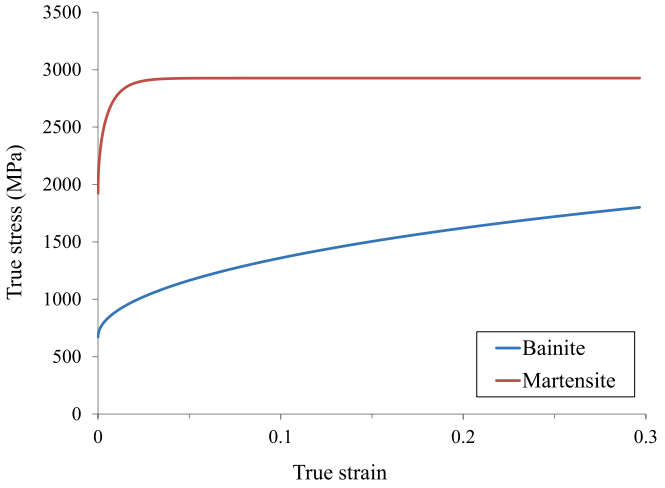

Fig. 5. Stress strain curves for bainite and martensite in B360.

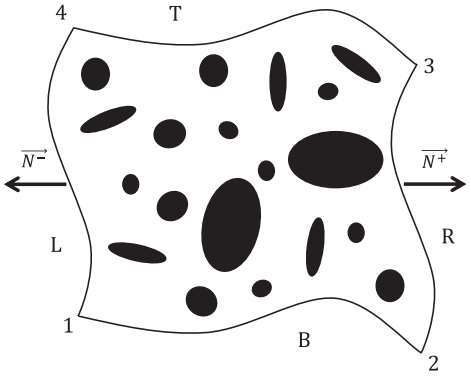

Fig. 6. The representation of PBCs.

data of the microstructure. This geometry as a periodic volume element is defined by the size and the grid in each direction. The size is chosen as 35 × 47.3 × 0.1 µms with 350 × 473 × 1 grid points to solve the equations. The information regarding grains belonging to different constituents which have different constitutive behaviors and also exist in various crystallographic orientations was also obtained from EBSD map in order to create the material model input. This geometry and material model information were then introduced to DAMASK. The tensile deformation was applied in x-direction (Fig. 2) with the strain rate of $6 \times 10^{-4}\ s^{-1}$ up to total strain of 0.09. The constitutive behavior of material is discussed in more detail in the following.

A phonemenological crystal plasticity material model together with a spectral solver has been used to model the tensile deformation

behavior and strain partitioning in the carbide free bainitic B360 steel. Crystal plasticity was implemented within DAMASK [65]. Among the material models [91–94] a viscoplastic phenomenological model [94] was chosen. The most important relations of this constitutive model are presented.

The deformation gradient $\boldsymbol{F}$ is decomposed multiplicatively to elastic and plastic parts:

$$\boldsymbol{F} = \boldsymbol{F}_e \boldsymbol{F}_p \tag{8}$$

where $\boldsymbol{F}_e$ describes the elastic deformation gradient which considers the elastic distortion of the lattice and $\boldsymbol{F}_p$ represents plastic deformation gradient which considers the cumulative effect of dislocation motion on the active slip systems in the crystal.

The plastic deformation evolves as:

$$\dot{\boldsymbol{F}}_p = \boldsymbol{L}_p \boldsymbol{F}_p \tag{9}$$

The plastic velocity gradient $\boldsymbol{L}_p$ is presented as a sum of all shear slips on slip systems:

$$\boldsymbol{L}_p = \sum_{\alpha=1}^{n} \dot{\gamma}^{\alpha} (\boldsymbol{m}^{\alpha} \otimes \boldsymbol{n}^{\alpha}) \tag{10}$$

where $\dot{\gamma}$ is the reference shear strain rate and α is the slip system index, vectors $\boldsymbol{m}^{\alpha}$ and $\boldsymbol{n}^{\alpha}$ are unit vectors which represent slip direction and normal to the slip plane respectively.

Phenomenological power law uses the critical shear stress S^{α} of the slip systems as state variable for each slip system α. The evolution of material state on slip system α is formulated as a function of total shear γ and shear rate $\dot{\gamma}^{\alpha}$. Given a set of current slip resistances, shear on each system evolves at a rate:

$$\dot{\gamma}^{\alpha} = \dot{\gamma}_0 \mathrm{sgn}(\tau^{\alpha}) \left(\frac{|\tau^{\alpha}|}{R^{\alpha}}\right)^{m} \tag{11}$$

where $\dot{\gamma}_0$ is reference shear rate, m is the strain rate exponent value, τ^{α} is resolved shear stress and R^{α} is current slip resistance of slip system α.

The resolved shear stress on slip system α is defined by:

$$\tau^{\alpha} = \boldsymbol{F}_e^{T} \boldsymbol{F}_e \boldsymbol{S} . (\boldsymbol{m}^{\alpha} \otimes \boldsymbol{n}^{\alpha}) \tag{12}$$

where $\boldsymbol{S}$ is considered as second Piola-Kirchhoff stress. As for metallic materials the elastic deformation is small, above equation is usually approximated as:

$$\tau^{\alpha} = \boldsymbol{S} . (\boldsymbol{m}^{\alpha} \otimes \boldsymbol{n}^{\alpha}) \tag{13}$$

In crystal plasticity theories, the slip system resistance parameter R^{α} is given by:

$$\dot{R}^{\alpha} = \sum_{\alpha=1}^{n} \dot{\gamma}^{\alpha} h_0 \left| 1 - \frac{R^{\alpha}}{R_s^{\alpha}} \right|^{a} \mathrm{sgn}\left(1 - \frac{R^{\alpha}}{R_s^{\alpha}}\right) h_{\alpha\beta} \tag{14}$$

where R_s^{α} is the saturation slip resistance, h_0 is the initial hardening rate, $h_{\alpha\beta}$ is the interaction parameter which describes the rate of increase of deformation resistance on slip system α due to shearing on slip system β and a is a fitting parameter. In this formula h_0, a, R_s^{α} are slip hardening parameters and are assumed to be identical for all slip systems.

To calibrate the material model parameters, the stress–strain curves for bainite and martensite were used (Fig. 5). Initial and saturation flow stress and parameters controlling the hardening behavior were estimated using reverse engineering, i.e. the effect of each single model parameter was studied in the simulation results to see which set of parameters results in the best fit with the calculated stress–strain response.

Using Voronoi tessellation algorithm [95] a randomized three dimensional microstructure was generated in order to approximate the distribution of grain size and shape. Periodic boundary conditions were imposed on this RVE. In order to find the suitable number of grains for this RVE, the stress–strain response of the simulations with different number of grains, were compared. Before any plastic strain develops, all the different analyses have the same response because of the elastic behavior of the grains and therefore there is no influence of the crystal orientations i.e. the model can be considered homogeneous. It was noted that the difference between the plastic responses is decreased when the number of grains is increased. In a model with more grains, the heterogeneity in the model tends to become less pronounced, which results in a more representative model for the macroscopic material. After the number of grains reaches a certain level, differences in texture do not cause much difference in the stress–strain response. The same load was applied on the RVE as in the macroscopic uniaxial tensile tests. Resolution was chosen to be 32 × 32 × 32 since the obtained results had no significant difference with the results from using an RVE with 64 × 64 × 64 resolution. For solving the equations an FFT solver was used [66].

The elastic properties for martensite are considered the same as in [36] and for bainite these were considered the same as for the B360 steel during the macroscopic tensile testing [68]. The calibrated material parameters are presented in Table 2.

2.3. In-situ tensile experiment

To analyze the strain partitioning and damage initiation in low carbon carbide free bainitic B360 steel, *in-situ* μDIC tensile experiment was performed in SEM. This experiment was combined with EBSD measurements prior to the *in-situ* testing [72]. Specimens with dimensions of 1 mm × 0.5 mm × 0.5 mm were deformed with a strain rate of 6×10^{-4} s^{-1} up to 9% global strain [72]. Electrical Discharge Machining (EDM) was used for sample preparation. Surfaces of the specimens were polished using colloidal silica (with 50–100 nm particle size).

In order to find the regions of interest (ROI) on the specimen surfaces a JEOL JSM 6500F scanning electron microscope was used. For the EBSD, accelerating voltage of 15 kV with a working distance of 18 mm and step size of 40 nm in a hexagonal scan grid were used. To locate the ROI during the *in-situ* testing, it was marked using Focused Ion Beam (FIB) milling in a Helios NanoLab 600i microscope. In order to perform local strain measurements during the tensile straining a monolayer of SiO2 particles (50–100 nm) was dispersed on the sample surface [72]. A Kammrath & Weiss stage inside the Zeiss Crossbeam XB 1540 microscope was used for *in-situ* tensile experiment. The deformation was applied on the specimens at a cross head speed of 3 μm/sec. After every deformation step of 1 μm, high resolution images of the ROI were taken using in-lens secondary electron (SE) detector. These images were then used for measurement of the von Mises equivalent micro-strain, using the Aramis software.

Table 2
The material parameters in phenomenological power law model for bainite and martensite.

Material parameters	Description	Bainite	Martensite
C_{11}	Elastic constant	282×10^3	417.4×10^3 MPa
C_{12}	Elastic constant	121×10^3	242.4×10^3 MPa
C_{44}	Elastic constant	80×10^3	211.1×10^3 MPa
$\dot{\gamma}_0$	Reference shear strain rate	0.001	0.001 ms^{-1}
R_0^{α}	Slip resistance	260	710 MPa
R_s^{α}	Saturation slip resistance	840	1140 MPa
h_0	Initial hardening rate	9×10^3	230×10^3 MPa
$h_{\alpha\beta}$	Interaction parameter	1	1
m	Strain rate exponent	20	20
a	Hardening exponent	3.2	2.05

3. Numerical simulation results

3.1. von Mises J2 plasticity finite element model (VPFEM)

The RVE as discussed in section 2.2.1. and the material properties which were calculated in section 2.2.2. were used together with a von Mises J2 plastic material model from Abaqus. The periodic boundary conditions (as discussed in section 2.2.3) were assigned to the RVE together with a tensile deformation applied in x-direction (Fig. 2) with strain rate of 6×10^{-4} s^{-1} up to total strain of 0.09. Fig. 7 shows the numerical simulation results of VPFEM performed in Abaqus. Fig. 7(a) illustrates the RVE used for this model. The regions which include bainite (B), martensite (M) and an island which contains a mixture of lath bainitic ferrite (LBF) and martensite (M) which is located in the upper left corner of this image, are shown.

The von Mises strain distributions at different levels of global strain at 2.7%, 4.7% and 9% are shown at Fig. 7(b)-Fig. 7(d). As can be observed, the von Mises strain is partitioned between different constituents and as a result, areas of strain concentration are created in the microstructure during tensile deformation. The analysis of the data shown in Fig. 7(d) while considering the RVE at Fig. 7(a), shows that these strain concentrations mostly occur in channels of bainite between martensitic islands. The high strain in the bainitic areas locally deforms the bainite while martensite does not accumulate much strain and local deformation.

Strain partitioning in these different regions vs the global strain is shown in Fig. 7(e). The von Mises local strain build up and partitioning in different constituents occurs while increasing the global strain. In order to measure these local strains, the average von Mises strain was measured in ten different elements from each constituent. The bainite (or bainitic ferrite) takes higher strain than the martensite. The bainite which is located in narrow channels between martensitic islands, takes much larger strains than bainite which is away from these channels and martensite islands. Therefore, the bainitic channels which are close to the martensitic regions face high strain localization. The narrower these channels are, the higher the strain localization will be. In Fig. 7(e), narrow bainite channels were considered to be the ones narrower than 5 μm while bainite distant from martensite, refers to channels wider than 5 μm. Using VPFEM, the average von Mises local strain was calculated to be 32.9 ± 1.1% in narrow channels (at 9.0% global strain) and 17.2 ± 0.8% in bainite channels wider than 5 μm (also shown in Table 3).

From the simulation, it can be seen that the local strains are concentrated along 45° angle to the tensile axis, which is aligned with the maximum resolved shear stress direction. Experimentally, we observed that the interfaces (of two adjacent bainitic ferrite grains) which are aligned in the direction of maximum resolved shear stress, show high strain accumulation compared to interfaces aligned in other directions. Therefore, these interfaces can be potential sites for damage

Table 3
The average local strain (%) built up at 9% global strain, in bainitic ferrite channels narrower or wider than 5 μm from simulations results and in-situ experiment results.

	Average local strain at bainitic channels < 5 μm	Average local strain at bainitic channels > 5 μm
VPFEM	32.9 ± 1.1%	17.2 ± 0.8%
CPFFT	30.7 ± 0.9%	18.1 ± 0.6%
In-situ experiment	30.4 ± 1.6%	20.5 ± 1.0%

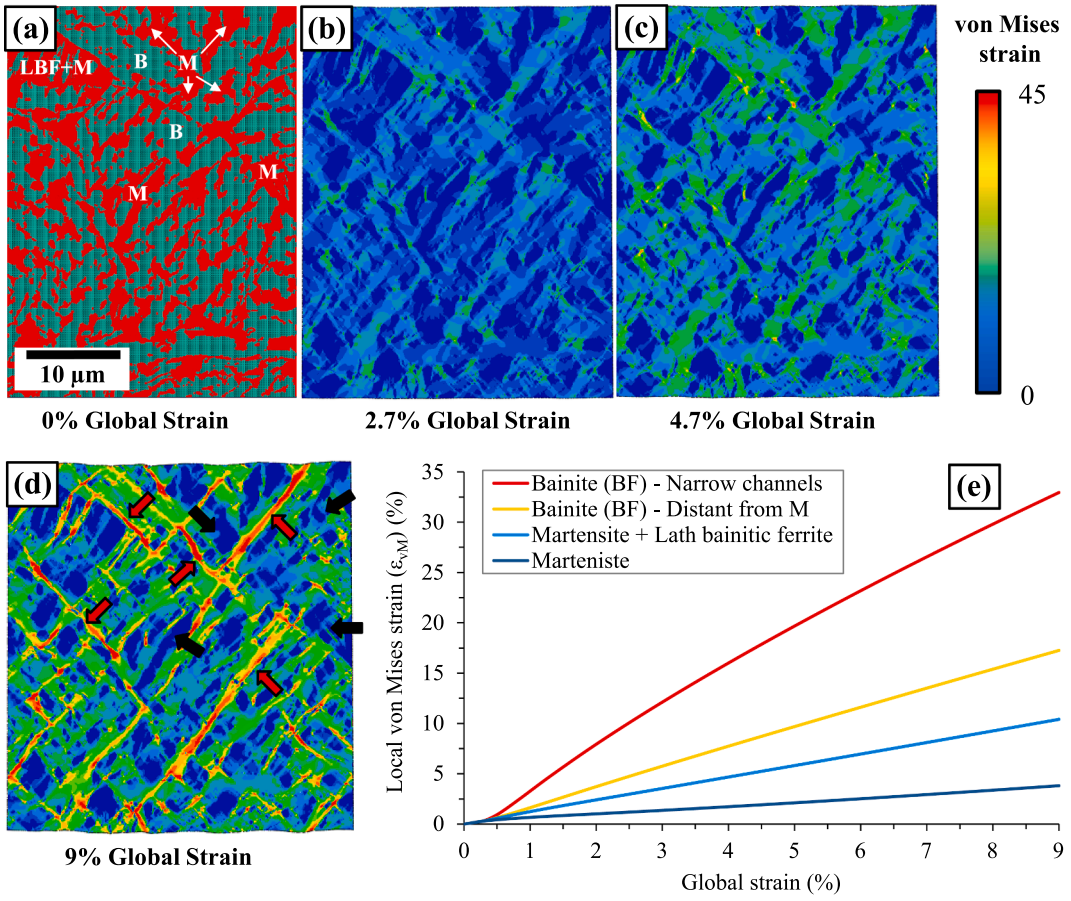

Fig. 7. VPFEM numerical simulation results, (a) The RVE used for this model, (b) Local strain map at 2.7% global strain, (c) Local strain map at 4.7% global strain, (d) Local strain map at 9 % global strain, (e) Strain partitioning among different constituents (and regions).

initiation [72].

The average strain accumulation in the islands with mixture of marteniste and LBF is lower than the average strain in the bainite regions while it is higher than the average strain accumulated in martensite. This is due to higher dislocation density and carbon concentration in LBF compared to coarse bainitic ferrite (in the bainite) [81]. In addition, this LBF is adjacent to martensite which gives this mixture more strength against straining.

The complex morphology of the carbide free bainitic steel makes it difficult to anticipate these strain concentration areas before loading. VPFEM gives an estimate of the strain concentration in the B360 microstructure. The maximum von Mises strain was measured to be 45% at 9.0% global strain (which happened in the upper right corner area in Fig. 7(d)). As a conclusion, the main reason for high strain localization in the microstructure of this carbide free bainitic steel is that martensite accommodates lower von Mises local strain compared to bainite. This causes high strain accumulation in narrow channels of bainite in between these marteniste islands. In Fig. 7(d), the red arrows indicate the high strain localization areas while the dark arrows represent the low strain areas occuring at martensitic islands. The areas indicated with red arrows could be candidates for nucleation of microcracks. As another damage initiating factor, martensite could also fracture in lower strains (compared to bainite), however as it was observed from numerical simulation, the critical value of fracture strain for martensite is not simply reached and the local strain rather partitions mostly into bainite.

3.2. Phenomenological crystal plasticity fast fourier transform model (CPFFT)

DAMASK modeling platform was also used to analyse the strain partitioning in the same sample. The calibrated material model parameters were assigned to the phenomenological model (as discussed in section 2.2.4.) and the same tensile deformation was applied.

Fig. 8 shows the CPFFT simulation results. In Fig. 8(a), the used RVE and the regions with different constituents are illustrated. Fig. 8(b)-(d) show the von Mises local strain build up during different stages of global strain at 2.7%, 4.7% and 9%. An observation similar to the one for VPFEM is also noted for CPFFT model i.e. the bainite endures much higher strain compared to martensite. This strain partitioning between different phases causes deformation localization in bainitic phase in between martensitic islands. In Fig. 8(d), the high strain concentration areas (in bainitic phase) are illustrated with red arrows and low strain areas in martensitic phase are shown with black arrows. As shown in this figure the strain is mostly localized in the bainite phase in between martensitic islands. These narrow bainitic channels in between martensite islands take more strain than the bainite in wider channels as shown in Fig. 8(e). At 9% global strain, the channels narrower than 5 μm take 30.7 ± 0.9% average local von Mises strain while bainitic channels wider than 5 μm take 18.1 ± 0.6% local strain (as shown also in Table 3). Hence, these narrow regions of bainite situated between the martensitic islands face the highest strain localization and can be considered as potential microcracks nucleation sites. The same as for VPFEM, the strains are localized in direction of 45° to the tensile direction, which is the same direction for maximum resolved shear stress.

Another influential parameter for strain localization is the

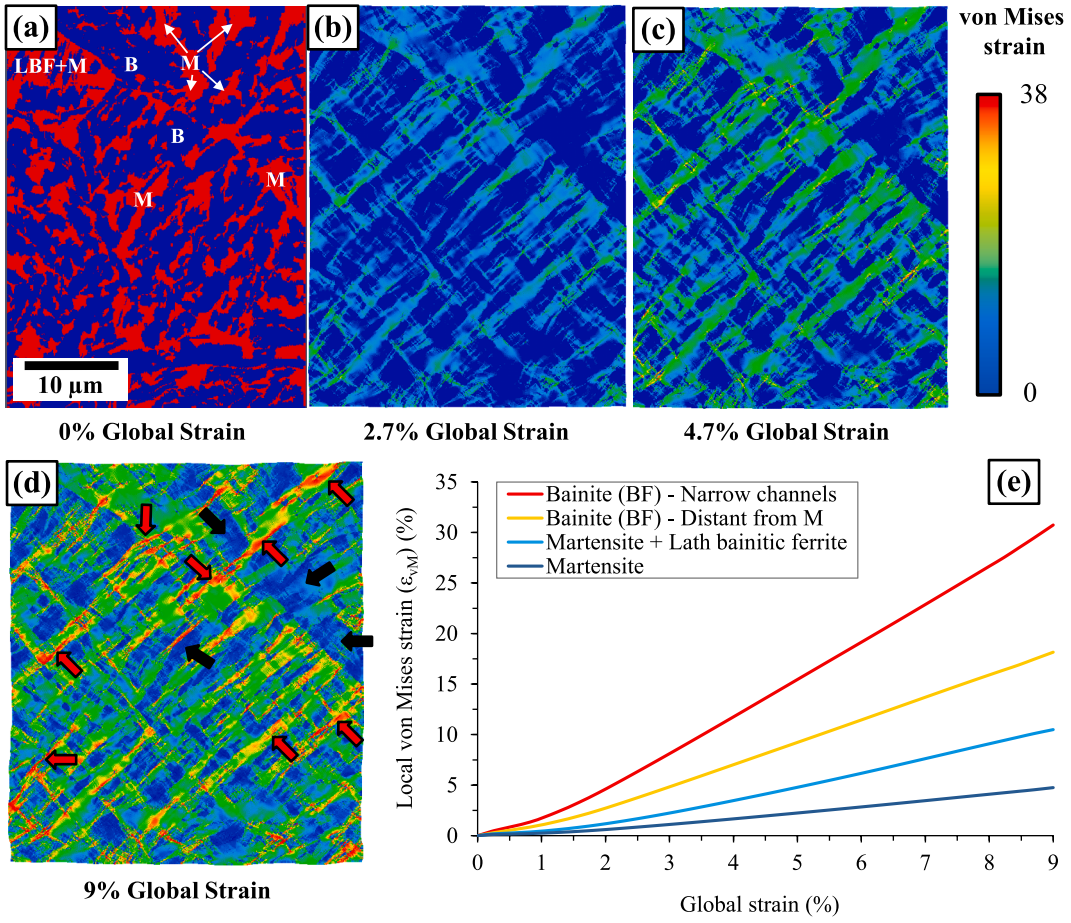

Fig. 8. CPFFT numerical simulation results, (a) The used RVE for this model, (b) Local strain map at 2.7% global strain, (c) Local strain map at 4.7% global strain, (d) Local strain map at 9% global strain, (e) Strain partitioning among different constituents (and regions).

inclination of the interfaces of two adjacent bainitic ferrite (in the bainite). In-line with the experimental observation [72], the interfaces aligned in the direction of maximum resolved shear stresses (i.e. 45° to the tensile direction) show high strain localization and can be potential sites for damage initiation.

There is a good agreement between CPFFT simulation results with the ones from VPFEM although some deviations can be observed. Both simulation results indicate that the main reason for the start of strain localization in the carbide free bainitic B360 steel is the much lower local von Mises strain built up in martensite compared to bainite. The areas with high possibility of microcrack initiation are mostly the same in both simulations (comparing Figs. 7(d) and 8(d)) although some deviation are also observed. For the CPFFT, the maximum von Mises at 9% global strain was estimated to be 38% in comparison to the 45% resulted from VPFEM simulation results. The maximum von Mises strain estimated by CPFFT is closer to the value captured from in-situ tensile experiment (which will be discussed in the following section). The more accurate strain localization from the CPFFT can be due to the more accurate material model and also consideration of the texture as a material input in this model.

4. The *in-situ* tensile test results

Fig. 9 shows the *in-situ* tensile test results performed on the B360 steel as described at section 2.3. Fig. 9(a) shows the overlapped EBSD phase map and IQ map of B360 steel with red color assigned to bainitic phase (B), green color assigned to BRA and black representing the low IQ areas indicating the martensitic islands (M). Fig. 9 s

Fig. 9(b)-(d) show the von Mises strain maps during different steps of global strains at 2.7%, 4.7% and 9%. In order to understand the strain partitioning behavior, the average local von Mises strain vs global strain for different constituents, are presented in Fig. 9(e). Martensite takes the lowest average von Mises strain. The local von Mises strain build up in the island with mixture of LBF and marteniste is larger than strains in the martensite due to presence of bainitic ferrtite laths but lower strain than BRA (as observed in Fig. 9(e)). Much less strain is accumulated in this island than the bainite. The higher dislocation density and carbon concentration in LBF compared to coarse bainitic ferrite (in the bainite) [81] together with the fact that this bainitic ferrite is mixed with stronger martensite result in lower strain build up in this constituent compared to bainite.

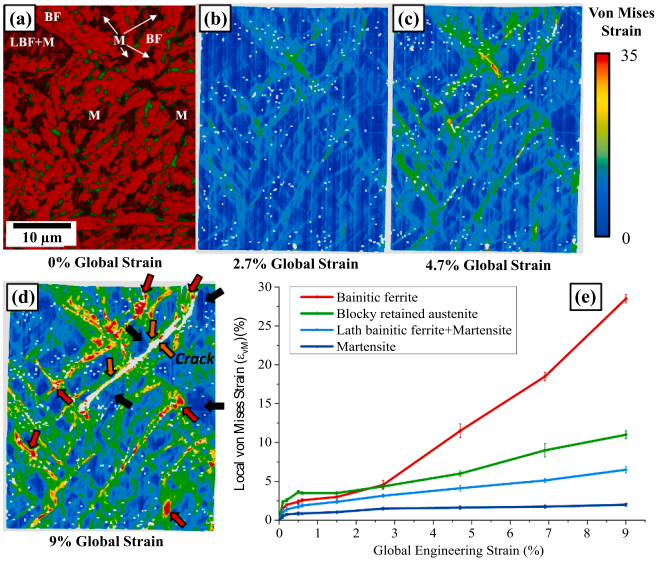

Fig. 9. In-situ tensile test results of B360 [72], (a) The EBSD map of the used microstructure, (b) Local strain map at 2.7% global strain, (c) Local strain map at 4.7% global strain, (d) Local strain map at 9% global strain, (e) Strain partitioning among different constituents.

BRA also tends to take more strain than martensite but less strain than the LBF and martensite mixture (at upper left corner in Fig. 9) and also the bainite. In the initial stages of global strain up to 2.3%, retained austenite takes the highest local strain among all other constituents. This can be due to the easy slip tendency in the face centered cubic crystal structure of retained austenite, which is followed by strain-induced transformation of austenite into martensite. As mentioned earlier in section 2.2.1. Another study on the same steel grade shows that the austenite fraction suddenly decreases during the global strain of 0 to 3% and the large BRA islands (grain size > 0.25 μm) which are less stable, turn into martensite [72]. After 2.3% of global strain, bainite takes the highest local von Mises strain among all the constituents. The maximum strain accumulation in BRA at 9% global strain is approximately 11%, which is still much lower than the 29% of average von Mises strain accumulated in bainite. This can be due to the fact that after 2.3% of global strain, BRA gradually further transforms into martensite by a strain-induced phase transformation which causes these locations to take less strain compared to untransformed retained austenite.

The strain partitioning causes strain localization mainly between martensitic islands in the bainite channels as it is depicted in Fig. 9(d). In this figure, the black arrows show the martensite islands (which take low strains) and the red arrows show the high strain concentration areas which are located in narrow bainite channels surrounded by martensitic areas. The orange arrows show the location of the crack in these channels which resulted from this excessive strain localization. This crack further continues and fractures the martensitic island in the middle of the microstructure. The test results show that the strains are higher when the bainitic ferrite channel is narrower. The average local strain was measured to be 30.4 ± 1.6% in bainitic ferrite channels narrower than 5 μm while this value was 20.5 ± 1.0% for channels which are wider than 5 μm. This confirms the good estimation from both simulations (as shown in Table 3).

As also observed for both simulations, the strain localization is maximum in the 45° angle to the tensile direction, which is aligned with the maximum resolved shear stress direction. The bainite-bainite interfaces which are oriented in the same direction (45° angle to the tensile direction) face the highest average von Mises strain and was measure to be 35% [72] in comparison to 45% using VPFEM and 38% using CPFFT.

There is general agreement between the simulation and experimental results. The microcrack observed at the *in-situ* tensile tests was among the possible crack locations predicted by both simulations. However, there are some deviations in the results which will be explained in more detail in the section 5.

The distribution of local von Mises strain obtained from both simulations and *in-situ* experiment at 9% global strain, are shown in Fig. 10. This figure shows the fraction of counts (or area fraction) for certain von Mises strain. These ditributions follow near-logarithmic shapes. At Fig. 10(a), the histogram resulted from Abaqus simulation shows that the highest area fraction occurs at strains of 2–6%. After these strains, the value of area fraction reduces fast until strains around 12% where the rate of this reduction decreases. This is due to the fact that a large fraction of bainite which are away from martensitic islands endure strains in the range of 13–20% (Fig. 7(e)). After local von Mises strains around 20% the area fraction value reduces rapidly in a logarithmic shape. According to DAMASK simulation results shown at Fig. 10(b), the area fraction reaches its peak at strains in the range of 4–8% and then this area fraction reduces rapidly until local strains in the range of 12–17% which are the strains accumulated at bainitic area which are located away from martensitic islands (Fig. 8(e)). In this strain range, the area fraction reduction rate decreases and after strains around 19% the area fraction value again reduces following a logarithmic pattern. Almost the same strain distribution is observed for *in-situ* simulation results as shown in Fig. 10(c), however after the peak of area fraction is reached, the it reduces in a more constant logarithmic rate compared to

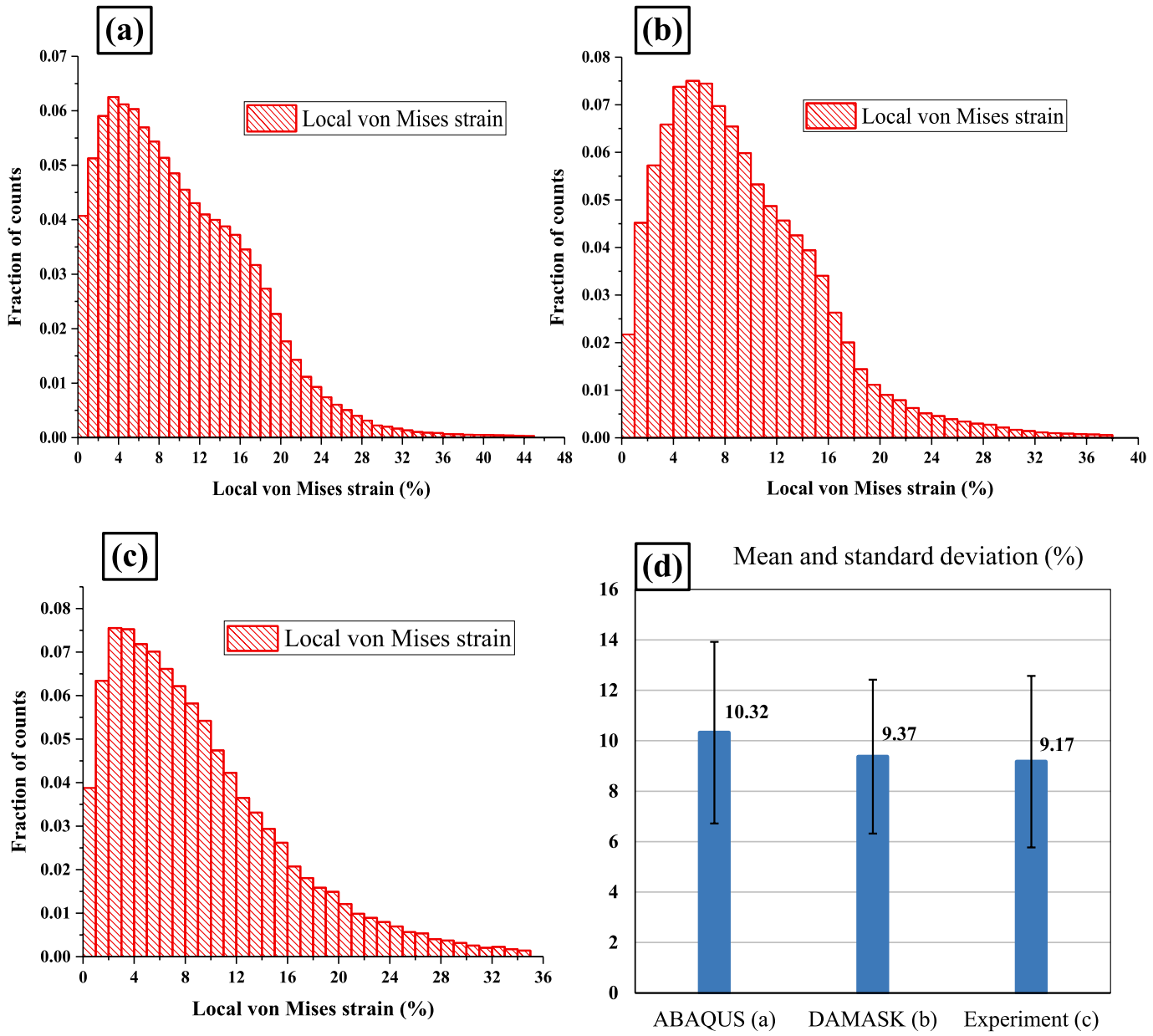

Fig. 10. Strain distribution at 9% global strain from experiment and numerical simulations; (a) ABAQUS simulation (VPFEM), (b) DAMASK simulation (CPFFT), (c) *in-situ* tensile test [72], (d) The mean and standard deviation (SD) of these distributions.

the simulation results. The maximum area fraction occurs at strains in the range of 2–7%. The main difference in local strain distribution results between simulation results and *in-situ* experiment is how the area fraction reduces fast after the peak is reached and then slows down for the strain ranges of 12–17% in numerical simulation results while for experiment results this distribution is more smooth. This could come from the fact that the BRA (which endure average local strain of around 11% in global strain of 9%) are not considered in the microstructure models (for the reasons explained in section 2.2.1.). Comparing the two modelling methods, it is observed that DAMASK simulation gives a better approximation of the local strain distribution from the experiments.

The mean and standard deviation (SD) of these distributions are calculated using a normal distribution (shown at Table 4 and Fig. 10(d)). The DAMASK simulation results show estimation of the local von Mises strain distribution closer to the experiment results (in comparison to the Abaqus simulation results).

Table 4
The mean and standard deviation (SD) of these distributions.

	Mean (%)	SD (%)
ABAQUS (a)	10.32	7.2
DAMASK (b)	9.37	6.1
Experiment (c)	9.17	6.8

5. Discussion

The observed localization patterns and strain concentration are indicators of damage initiation in the Continuously Cooled Carbide Free Bainitic Steels (CC-CFBS) or B360. The numerical simulations were performed in order to investigate the strain partitioning in B360, using a von Mises plastic finite element model (VPFEM) by Abaqus and also a phonemenological crystal plasticity with a fast Fourier transform solver (CPFFT) utilizing DAMASK. *In-situ* tensile experiment was performed in

order to validate the numerical simulation results and to observe damage initiating factors in B360. Both simulations and the experiment were performed on the same geometry. In the numerical simulations, the RVE was constructed based on the assumption that all the blocky retained austenite turns into martensite from the beginning of the straining. This is a simplification based on the fact a that large part of the large islands of BRA (grain size $>$ 0.25 μm) which are unstable, transform into martensite in a deformation induced martensitic transformation mechanism which results in reduction in the fraction of retained austenite fraction in the microstructure [72]. TFRA (inside the bainitic lath) and also the ultrafine islands of BRA (grain size $<$ 0.25 μm) are more stable [72,81,96–99] and do not transform into marteniste.

Simulated von Mises strain maps (Fig. 7 and Fig. 8) during different stages of tensile straining show a reasonable correlation with the *in-situ* experiment (Fig. 9). Based on both simulations, von Mises strain localization is mostly due to presence of large martensitic islands and large BRA (grain size $>$ 0.25 μm) which later transform into martenite in the microstructure. Very low degree of strain is endured by these martensitic islands and strain is localized in the narrow channels of bainite in the interfaces of martensite and bainitic ferrite. This is confirmed by *in-situ* tensile tests showing that there is strong strain concentration in bainite between martensitic islands and crack initiates from these interfaces of martensite and bainite and grows along the interfaces by fracturing of martensitic islands (Fig. 9(d)) [72]. The narrower these channels are the higher the strain accumulation is. Channels which are narrower than the threshold value of 5 μm, accumulate much higher local strains than the wider channels.

Both numerical simulations give an acceptable estimate of the damage initiation sites in the microstructure of B360. While VPFEM uses a simpler material model and does not take into account the texture of the steel microstructure, it gives a good estimate of the strain localization areas. However, there is difference in the maximum local von Mises strain estimated by the VPFEM and CPFFT simulation results compared to *in-situ* experiment. At 9% of global strain VPFEM and CPFFT simulations show 28.5% and 8.5% error in estimating maximum local von Mises strain, respectively. The geometry and texture information for the phenomenological crystal plasticity model are easy to obtain directly using the EBSD data, however the phenomenological material model parameters for each phase must be calibrated using macroscopic flow curves for each phase. The CPFFT model takes into account texture information of each grain and with a more complex and accurate material model so that it gives better approximation of the maximum von Mises local strain together with the locations of these strain localizations.

The histograms of the von Mises strain distribution in the microstructure were also calculated and compared. The histograms resulted from the simulations differ slightly from the histogram of the *in-situ* test, especially the one from VPFEM by Abaqus. Considering the histogram from *in-situ* test, after reaching the peak area fraction (strains of 2–4%), it reduces in a logarithmic pattern while for the simulation results the rate of reduction is low in the strain ranges 12–17% and then increases. In other words, the area fraction for strain of 7–13% are higher for the *in-situ* experiment results compared to the simulation results while the area fraction of strains in the range of 12–17% are higher for simulation results. This is because of several reasons, one of them being the simplification (in the numerical simulations) that all BRA transforms into martensite from the beginning of the straining. This simplification not only changes the area fraction of the local strains around 11% (average local strain enured by BRA) and shift it towards much lower strains (because we consider they turn into martensite), but also changes the phase morphology and creates more area fraction of strains in the range of 12–17%.

The deviations (of strain localization maps) observed among the numerical simulations results (Fig. 7(d), Fig. 8(d)) and the *in-situ* experiment (Fig. 9(d)) can also be the result of considering a two dimensional (2D) geometry instead of a three dimensional (3D) one. As an example, the left top corner of the specimen, with the LBF aggregated with martensite (shown by LBF + M in Figs. 7(a)-9(a)), shows that in both numerical simulations, there is strain localization in the bainitic ferrite in the middle of this region. However, such strain localization was not observed in the *in-situ* experiment. This could be because that other martensitic layers under or above this LBF do not allow this softer constituent to strain as much as we observe in the 2D numerical models. Accuracy in geometry and RVE creation would help to include more microstrutural details such as lamellar structure of bainite (bainitic ferrite and retained austenite). Higher resolution imaging can also help to capture more details of the microstructure.

Choosing suitable material model and measuring accurately the mechanical behavior and (also possibly) damage characteristics for each phase would result in more accurate numerical models. Using nano-indentation technique in order to characterize the mechanical properties of each phase would help to obtain a more accurate estimation of the strain partitioning and damage initiation in steels [36]. The martensitic phase transformation and the stability of the retained austenite during deformation have significant influence on the mechanical behavior and ductility of steels which experience this phenomenon [35]. Therefore, considering deformation-induced martensitic phase transformation in the numerical material models is another very important step in simulating the strain partitioning behavior of these steels.

In summary, in order to increase the accuracy of the numerical models, there is a need for accurate geometry and precise material behavior modelling, i.e. we should try to represent the actual behavior of each phase/constituent with a suitable material model which also includes precise model parameters.

The carbide free bainitic steels do not contain cementite laths like pearlitic steels. These cementite laths in pearlitic steels can lead to the formation of brittle white etching layer (WEL) due to cementite dissolution under plastic deformation [100,101]. This WEL could be related to rolling contact fatigue in the rails [102]. However the void formation by strain incompatibility between hard martensite and bainite, makes this steel vulnerable to damage under rolling contact loading conditions as well [103].

6. Conclusion and future work

Strain partitioning in Continuously Cooled Carbide Free Bainitic Steels (CC-CFBS) (B360) was simulated using von Mises J2 plasticity and also phenomenological crystal plasticity material models. Both models give reasonable estimation of the strain localization pheonomena compared to *in-situ* tensile experiment which was used to validate these numerical simulations. However, the phenomenological crystal plasticity model gives results closer to the *in-situ* tensile experiment than the von Mises plasticity model.

There were some deviations between the simulation results and the experiment, regarding the strain localization maps and also the maximum von Mises local strain estimation. These deviations could be due to simpler geometrical and material models considered in the model. For the geometry in the numerical models, a 2D RVE was used instead of a 3D microstructure. The retained austenite transfomation into martensite was neglected and the blocky retained austenite (BRA) was considered to transform into martensite at the beginning of the straining. This simplification was done since large BRA transform into martensite during loading in a strain-induced transformation mechanism. More accurate mechanical behavior modelling of each phase can be developed using more advanced methods such as nano-indentation. Considering damage characteristics of each phase, can help to obtain a more realistic material model.

Factors such as martensite/bainitic ferrite interfaces, interface orientation with respect to tensile direction, spatial distribution of phases, phase fraction and phase morphology influence the strain partitioning and damage initiation in this carbide free bainitic steel. The martensitic islands and the large BRA (which transform into martensite under strain) present in B360 steel, could initiate damage which in

general reduces the mechanical performance. The main damage mechanism in this steel is strain localization in the narrow channels of bainite and in the interfaces of bainite with martensite which later develops voids and eventually cracks which also leads to fracture of martensitic islands.

In order to design a better microstructure while benefitting from the absence of carbides, there is a need to improve this microstructure using the lessons learned from this research. To do so, elimination of large BRA and martensitic islands might help this steel to achieve better mechanical and damage characteristics.

CRediT authorship contribution statement

O. Hajizad: Conceptualization, Data curation, Formal analysis, Methodology, Software, Validation, Visualization, Writing – original draft, Writing – review & editing. **A. Kumar:** Data curation, Formal analysis, Investigation, Methodology, Visualization, Writing – review & editing. **R.H. Petrov:** Formal analysis, Funding acquisition, Project administration, Resources, Supervision, Writing – review & editing. **J. Sietsma:** Formal analysis, Funding acquisition, Project administration, Resources, Supervision, Writing – review & editing. **R. Dollevoet:** Formal analysis, Funding acquisition, Project administration, Resources, Supervision, Writing – review & editing. **Z. Li:** Formal analysis, Funding acquisition, Project administration, Resources, Supervision, Writing – review & editing.

Declaration of Competing Interest

The authors declare that they have no known competing financial interests or personal relationships that could have appeared to influence the work reported in this paper.

Acknowledgement

We would like to thank Dutch railway infrastructure manager, ProRail for the financial support of this project and also helping us with the specimen for the experimental validation part of this research. This research was partly carried out under project number T91.1.12475a in the framework of the resear ch program of the Materials innovation institute M2i (www.m2i.nl).The RVEs (used to calibrate the material models), was created using Voronoi diagram algorithm from the software created by Piet Kok from Tata Steel Europe and his help is appreciated and acknowledged.

References

[1] R. Dollevoet, Design of an anti-head check profile based on stress relief, 2016. doi:10.3990/1.9789036530736.
[2] R. Dollevoet, Z. Li, O. Arias-Cuevas, A method for the prediction of head checking initiation location and orientation under operational loading conditions, Proc. Inst. Mech. Eng. Part F J. Rail Rapid Transit. 224 (5) (2010) 369–374, https://doi.org/10.1243/09544097JRRT368.
[3] Z. Li, X. Zhao, C. Esveld, R. Dollevoet, M. Molodova, An investigation into the causes of squats-Correlation analysis and numerical modeling, Wear. 265 (9-10) (2008) 1349–1355, https://doi.org/10.1016/j.wear.2008.02.037.
[4] W.J. Jiang, C. Liu, C.G. He, J. Guo, W.J. Wang, Q.Y. Liu, Investigation on impact wear and damage mechanism of railway rail weld joint and rail materials, Wear. 376–377 (2017) 1938–1946, https://doi.org/10.1016/j.wear.2017.02.035.
[5] R. Lewisa, R.S. Dwyer-Joyce, Wear mechanisms and transitions in railway wheel steels, Proc. Inst. Mech. Eng. Part J J. Eng. Tribol. 218 (6) (2004) 467–478, https://doi.org/10.1243/1350650042794815.
[6] K.M. Lee, A.A. Polycarpou, Wear of conventional pearlitic and improved bainitic rail steels, Wear. 259 (1-6) (2005) 391–399, https://doi.org/10.1016/j.wear.2005.02.058.
[7] H.A. Aglan, Z.Y. Liu, M.F. Hassan, M. Fateh, Mechanical and fracture behavior of bainitic rail steel, J. Mater. Process. Technol. 151 (1-3) (2004) 268–274, https://doi.org/10.1016/j.jmatprotec.2004.04.073.
[8] H.K.D.H. Bhadeshia, High performance bainitic steels, Mater. Sci. Forum. 500–501 (2005) 63–74, https://doi.org/10.4028/www.scientific.net/MSF.500-501.63.
[9] T. Suzuki, Y. Ono, G. Miyamoto, T. Furuhara, Effects of Si and Cr on bainite microstructure of medium carbon steels, ISIJ Int. 50 (10) (2010) 1476–1482, https://doi.org/10.2355/isijinternational.50.1476.
[10] X.Y. Long, J. Kang, B. Lv, F.C. Zhang, Carbide-free bainite in medium carbon steel, Mater. Des. 64 (2014) 237–245, https://doi.org/10.1016/j.matdes.2014.07.055.
[11] H.K.D.H. Bhadeshia, Nanostructured bainite, Proc. R. Soc. A Math Phys. Eng. Sci. 466 (2010) 3–18, https://doi.org/10.1098/rspa.2009.0407.
[12] H.K.D.H. Bhadeshia, The first bulk nanostructured metal, Sci. Technol. Adv. Mater. 14 (2013), https://doi.org/10.1088/1468-6996/14/1/014202.
[13] F.G. Caballero, C. Garcia-Mateo, M.K. Miller, Design of novel bainitic steels: moving from ultrafine to nanoscale structures, Jom. 66 (2014) 747–755, https://doi.org/10.1007/s11837-014-0908-0.
[14] K.-H. Kim, J.-S. Lee, On microstructure and properties of Si modified 100Cr6 bearing steels, Mater. Sci. Technol. 28 (1) (2012) 50–54, https://doi.org/10.1179/1743284711Y.0000000053.
[15] X. Gui, K. Wang, G. Gao, R.D.K. Misra, Z. Tan, B. Bai, Rolling contact fatigue of bainitic rail steels: the significance of microstructure, Mater. Sci. Eng. A. 657 (2016) 82–85, https://doi.org/10.1016/j.msea.2016.01.052.
[16] K. Chung, N. Ma, T. Park, D. Kim, D. Yoo, C. Kim, A modified damage model for advanced high strength steel sheets, Int. J. Plast. 27 (10) (2011) 1485–1511, https://doi.org/10.1016/j.ijplas.2011.01.007.
[17] M. Brünig, S. Gerke, V. Hagenbrock, Stress-state-dependence of damage strain rate tensors caused by growth and coalescence of micro-defects, 63 (2014) 49–63. doi:10.1016/j.ijplas.2014.04.007.
[18] L. Malcher, E.N. Mamiya, An improved damage evolution law based on continuum damage mechanics and its dependence on both stress triaxiality and the third invariant, Int. J. Plast. 56 (2014) 232–261, https://doi.org/10.1016/j.ijplas.2014.01.002.
[19] M. Brünig, S. Gerke, Simulation of damage evolution in ductile metals undergoing dynamic loading conditions, 27 (2011) 1598–1617. doi:10.1016/j.ijplas.2011.02.003.
[20] M. Brünig, S. Gerke, V. Hagenbrock, Micro-mechanical studies on the effect of the stress triaxiality and the Lode parameter on ductile damage, Int. J. Plast. 50 (2013) 49–65, https://doi.org/10.1016/j.ijplas.2013.03.012.
[21] M. Brünig, O. Chyra, D. Albrecht, L. Driemeier, M. Alves, A ductile damage criterion at various stress triaxialities, 24 (2008) 1731–1755. doi:10.1016/j.ijplas.2007.12.001.
[22] J.V.S. Cavalheiro, L. Malcher, Assessment of third invariant elasto-plastic models_ Mathematical aspects, numerical strategies and comparative results, Finite Elem. Anal. Des. 123 (2017) 51–69, https://doi.org/10.1016/j.finel.2016.09.001.
[23] L. Malcher, F.M.A. Pires, J.M.A.C. De Sá, An extended GTN model for ductile fracture under high and low stress triaxiality, Int. J. Plast. 54 (2014) 193–228, https://doi.org/10.1016/j.ijplas.2013.08.015.
[24] J.Q. Ran, M.W. Fu, A hybrid model for analysis of ductile fracture in micro-scaled plastic deformation of multiphase alloys, 61 (2014) 1–16. doi:10.1016/j.ijplas.2013.11.006.
[25] M. Basirat, T. Shrestha, G.P. Potirniche, I. Charit, K. Rink, A study of the creep behavior of modified 9Cr – 1Mo steel using continuum-damage modeling, Int. J. Plast. 37 (2012) 95–107, https://doi.org/10.1016/j.ijplas.2012.04.004.
[26] C.F.B. Sandoval, L. Malcher, F.A. Canut, L.M. Araújo, T.C.R. Doca, J.A. Araújo, Micromechanical Gurson-based continuum damage under the context of fretting fatigue: influence of the plastic strain field, Int. J. Plast. (2019), https://doi.org/10.1016/j.ijplas.2019.09.012.
[27] J. Kim, J. Whan, Necking behavior of AA 6022–T4 based on the crystal plasticity and damage models, Int. J. Plast. 73 (2015) 3–23, https://doi.org/10.1016/j.ijplas.2015.06.013.
[28] M. Knezevic, I.J. Beyerlein, D.W. Brown, T.A. Sisneros, C.N. Tomé, A polycrystal plasticity model for predicting mechanical response and texture evolution during strain-path changes: application to beryllium, Int. J. Plast. 49 (2013) 185–198, https://doi.org/10.1016/j.ijplas.2013.03.008.
[29] A.S. Khan, J. Liu, J. Whan, R. Nambori, Strain rate effect of high purity aluminum single crystals: experiments and simulations, Int. J. Plast. 67 (2015) 39–52, https://doi.org/10.1016/j.ijplas.2014.10.002.
[30] M. Ardeljan, I.J. Beyerlein, M. Knezevic, Journal of the Mechanics and Physics of Solids A dislocation density based crystal plasticity finite element model: application to a two-phase polycrystalline HCP / BCC composites, J. Mech. Phys. Solids. 66 (2014) 16–31, https://doi.org/10.1016/j.jmps.2014.01.006.
[31] M. Knezevic, H.F. Al-Harbi, S.R. Kalidindi, Crystal plasticity simulations using discrete Fourier transforms, Acta Mater. 57 (6) (2009) 1777–1784, https://doi.org/10.1016/j.actamat.2008.12.017.
[32] P. Hu, Y. Liu, Y. Zhu, L. Ying, Crystal plasticity extended models based on thermal mechanism and damage functions: application to multiscale modeling of aluminum alloy tensile behavior, Int. J. Plast. 86 (2016) 1–25, https://doi.org/10.1016/j.ijplas.2016.07.001.
[33] J. Ha, J. Lee, J. Hoon, M. Lee, Investigation of plastic strain rate under strain path changes in dual-phase steel using microstructure-based modeling d e, 93 (2017). doi:10.1016/j.ijplas.2017.02.005.
[34] X. Shang, H. Zhang, Z. Cui, M.W. Fu, J. Shao, A multiscale investigation into the effect of grain size on void evolution and ductile fracture: Experiments and crystal plasticity modeling, (2019). 10.1016/j.ijplas.2019.09.009.
[35] K.S. Choi, W.N. Liu, X. Sun, M.A. Khaleel, Microstructure-based constitutive modeling of TRIP steel: prediction of ductility and failure modes under different loading conditions, Acta Mater. 57 (2009) 2592–2604, https://doi.org/10.1016/j.actamat.2009.02.020.

[36] C.C. Tasan, J.P.M. Hoefnagels, M. Diehl, D. Yan, F. Roters, D. Raabe, Strain localization and damage in dual phase steels investigated by coupled in-situ deformation experiments and crystal plasticity simulations, Int. J. Plast. 63 (2014) 198–210, https://doi.org/10.1016/j.ijplas.2014.06.004.

[37] K. Alharbi, H. Ghadbeigi, P. Efthymiadis, M. Zanganeh, S. Celotto, R. Dashwood, C. Pinna, Damage in dual phase steel DP1000 investigated using digital image correlation and microstructure simulation, Model. Simul. Mater. Sci. Eng. 23 (2015), https://doi.org/10.1088/0965-0393/23/8/085005.

[38] B. Berisha, C. Raemy, C. Becker, M. Gorji, P. Hora, Multiscale modeling of failure initiation in a ferritic – pearlitic steel, Acta Mater. 100 (2015) 191–201, https://doi.org/10.1016/j.actamat.2015.08.035.

[39] B. Erice, C.C. Roth, D. Mohr, Stress-state and strain-rate dependent ductile fracture of dual and complex phase steel, Mech. Mater. 116 (2018) 11–32, https://doi.org/10.1016/j.mechmat.2017.07.020.

[40] X. Sun, K.S. Choi, A. Soulami, W.N. Liu, M.A. Khaleel, On key factors influencing ductile fractures of dual phase (DP) steels, Mater. Sci. Eng. A. 526 (1-2) (2009) 140–149, https://doi.org/10.1016/j.msea.2009.08.010.

[41] X. Sun, K.S. Choi, W.N. Liu, M.A. Khaleel, Predicting failure modes and ductility of dual phase steels using plastic strain localization, Int. J. Plast. 25 (10) (2009) 1888–1909, https://doi.org/10.1016/j.ijplas.2008.12.012.

[42] A. Ramazani, M. Abbasi, S. Kazemiabnavi, S. Schmauder, R. Larson, U. Prahl, Development and application of a microstructure-based approach to characterize and model failure initiation in DP steels using XFEM, Mater. Sci. Eng. A. 660 (2016) 181–194, https://doi.org/10.1016/j.msea.2016.02.090.

[43] J. Kadkhodapour, S. Schmauder, D. Raabe, S. Ziaei-Rad, U. Weber, M. Calcagnotto, Experimental and numerical study on geometrically necessary dislocations and non-homogeneous mechanical properties of the ferrite phase in dual phase steels, Acta Mater. 59 (11) (2011) 4387–4394, https://doi.org/10.1016/j.actamat.2011.03.062.

[44] J. Kadkhodapour, A. Butz, S. Ziaei-Rad, S. Schmauder, A micro mechanical study on failure initiation of dual phase steels under tension using single crystal plasticity model, Int. J. Plast. 27 (7) (2011) 1103–1125, https://doi.org/10.1016/j.ijplas.2010.12.001.

[45] D. Kim, E. Kim, J. Han, W. Woo, S. Choi, Effect of microstructural factors on void formation by ferrite / martensite interface decohesion in DP980 steel under uniaxial tension, Int. J. Plast. 94 (2017) 3–23, https://doi.org/10.1016/j.ijplas.2017.04.019.

[46] A. Das, S. Tarafder, S. Sivaprasad, D. Chakrabarti, Infl uence of microstructure and strain rate on the strain partitioning behaviour of dual phase steels, Mater. Sci. Eng. A. 754 (2019) 348–360, https://doi.org/10.1016/j.msea.2019.03.084.

[47] T. Matsuno, C. Teodosiu, D. Maeda, A. Uenishi, Mesoscale simulation of the early evolution of ductile fracture in dual-phase steels, Int. J. Plast. 74 (2015) 17–34, https://doi.org/10.1016/j.ijplas.2015.06.004.

[48] A.C. Darabi, H.R. Chamani, J. Kadkhodapour, A.P. Anaraki, A. Alaie, M.R. Ayatollahi, Mechanics of Materials Micromechanical analysis of two heat-treated dual phase steels: DP800 and DP980, 110 (2017) 68–83.

[49] J. Hoon, D. Kim, F. Barlat, M. Lee, Crystal plasticity approach for predicting the Bauschinger effect in dual-phase steels, Mater. Sci. Eng. A. 539 (2012) 259–270, https://doi.org/10.1016/j.msea.2012.01.092.

[50] C.C. Roth, T.F. Morgeneyer, Y. Cheng, L. Helfen, D. Mohr, Ductile damage mechanism under shear-dominated loading: in-situ tomography experiments on dual phase steel and localization analysis, Int. J. Plast. 109 (2018) 169–192, https://doi.org/10.1016/j.ijplas.2018.06.003.

[51] N. Fujita, N. Ishikawa, F. Roters, C.C. Tasan, D. Raabe, Experimental-numerical study on strain and stress partitioning in bainitic steels with martensite-austenite constituents, Int. J. Plast. 104 (2018) 39–53, https://doi.org/10.1016/j.ijplas.2018.01.012.

[52] U. Liedl, S. Traint, E.A. Werner, An unexpected feature of the stress–strain diagramof dual-phase steel, 25 (2002) 122–128.

[53] Z. Zhao, M. Ramesh, D. Raabe, A.M. Cuitiño, R. Radovitzky, Investigation of three-dimensional aspects of grain-scale plastic surface deformation of an aluminum oligocrystal, Int. J. Plast. 24 (12) (2008) 2278–2297, https://doi.org/10.1016/j.ijplas.2008.01.002.

[54] L. Wang, R.I. Barabash, Y. Yang, T.R. Bieler, M.A. Crimp, P. Eisenlohr, W. Liu, G. E. Ice, Experimental characterization and crystal plasticity modeling of heterogeneous deformation in polycrystalline α-Ti, Metall. Mater. Trans. A Phys. Metall. Mater. Sci. 42 (3) (2011) 626–635, https://doi.org/10.1007/s11661-010-0249-8.

[55] S.-H. Choi, E.-Y. Kim, W. Woo, S.H. Han, J.H. Kwak, The effect of crystallographic orientation on the micromechanical deformation and failure behaviors of DP980 steel during uniaxial tension, 45 (2013) 85–102. doi:10.1016/j.ijplas.2012.11.013.

[56] D. Cédat, O. Fandeur, C. Rey, D. Raabe, Polycrystal model of the mechanical behavior of a Mo-TiC30vol.% metal-ceramic composite using a 3D microstructure map obtained by a dual beam FIB-SEM, Acta Mater. 60 (2012) 1623–1632.

[57] J. Kang, Y. Ososkov, J. Embury, D. Wilkinson, Digital image correlation studies for microscopic strain distribution and damage in dual phase steels, Scr. Mater. 56 (11) (2007) 999–1002, https://doi.org/10.1016/j.scriptamat.2007.01.031.

[58] H. Ghadbeigi, C. Pinna, S. Celotto, J.R. Yates, Local plastic strain evolution in a high strength dual-phase steel, Mater. Sci. Eng. A. 527 (18-19) (2010) 5026–5032, https://doi.org/10.1016/j.msea.2010.04.052.

[59] M. Kapp, T. Hebesberger, O. Kolednik, A micro-level strain analysis of a high-strength dual-phase steel, Int. J. Mat. Res. 102 (2011) 687–691.

[60] J. Marteau, H. Haddadi, S. Bouvier, Investigation of strain heterogeneities between grains in ferritic and ferritic-martensitic steels, Exp. Mech. 53 (3) (2013) 427–439, https://doi.org/10.1007/s11340-012-9657-6.

[61] C.C. Tasan, J.P.M. Hoefnagels, M.G.D. Geers, Microstructural banding effects clarified through micrographic digital image correlation, Scr. Mater. 62 (2010) 835–838 (accessed November 15, 2018), https://pure.mpg.de/pubman/item/item_2015292_2.

[62] G. Martin, C.W. Sinclair, R.A. Lebensohn, Microscale plastic strain heterogeneity in slip dominated deformation of magnesium alloy containing rare earth, Mater. Sci. Eng. A. 603 (2014) 37–51, https://doi.org/10.1016/j.msea.2014.01.102.

[63] H. Lim, J.D. Carroll, C.C. Battaile, T.E. Buchheit, B.L. Boyce, C.R. Weinberger, Grain-scale experimental validation of crystal plasticity finite element simulations of tantalum oligocrystals, Int. J. Plast. 60 (2014) 1–18, https://doi.org/10.1016/j.ijplas.2014.05.004.

[64] C.C. Tasan, M. Diehl, D. Yan, C. Zambaldi, P. Shanthraj, F. Roters, D. Raabe, Integrated experimental-simulation analysis of stress and strain partitioning in multiphase alloys, Acta Mater. 81 (2014) 386–400, https://doi.org/10.1016/j.actamat.2014.07.071.

[65] F. Roters, P. Eisenlohr, C. Kords, D.D. Tjahjanto, M. Diehl, D. Raabe, DAMASK: the Düsseldorf Advanced MAterial Simulation Kit for studying crystal plasticity using an FE based or a spectral numerical solver, Procedia IUTAM. 3 (2012) 3–10, https://doi.org/10.1016/j.piutam.2012.03.001.

[66] R.A. Lebensohn, A.D. Rollett, P. Suquet, Fast Fourier transform-based modeling for the determination of micromechanical fields in polycrystals, Jom. 63 (3) (2011) 13–18, https://doi.org/10.1007/s11837-011-0037-y.

[67] H.-S. Yang, Design of Low-Carbon, Low-Temperature Bainite, 2011.

[68] O. Hajizad, A. Kumar, Z. Li, R.H. Petrov, J. Sietsma, Influence of Microstructure on Mechanical Properties of Bainitic Steels in Railway Applications, (2019) 1–19.

[69] A.W. Wilson, J.D. Madison, G. Spanos, Determining phase volume fraction in steels by electron backscattered diffraction, Scr. Mater. 45 (12) (2001) 1335–1340, https://doi.org/10.1016/S1359-6462(01)01137-X.

[70] J. Wu, P.J. Wray, C.I. Garcia, M. Hua, A.J. Deardo, Image quality analysis: a new method of characterizing microstructures, ISIJ Int. 45 (2005) 254–262, https://doi.org/10.2355/isijinternational.45.254.

[71] R. Hill, Elastic properties of reinforced solids: Some theoretical principles, J. Mech. Phys. Solids. 11 (5) (1963) 357–372, https://doi.org/10.1016/0022-5096(63)90036-X.

[72] A. Kumar, A. Dutta, S.K. Makineni, M. Herbig, R.H. Petrov, J. Sietsma, In-situ observation of strain partitioning and damage development in continuously cooled carbide-free bainitic steels using micro digital image correlation, Mater. Sci. Eng. A. 757 (2019) 107–116, https://doi.org/10.1016/j.msea.2019.04.098.

[73] M. Latypov, S. Shin, B. De Cooman, H. Kim, Micromechanical finite element analysis of strain partitioning in multiphase medium manganese TWIP+TRIP steel, 2016. doi:10.1016/j.actamat.2016.02.001.

[74] R.-M. Rodriguez, I. Gutiérrez, Unified formulation to predict the tensile curves of steels with different microstructures, Mater. Sci. Forum. 426–432 (2003) 4525–4530, https://doi.org/10.4028/www.scientific.net/MSF.426-432.4525.

[75] Y. Bergström, A dislocation model for the stress-strain behaviour of polycrystalline α-Fe with special emphasis on the variation of the densities of mobile and immobile dislocations, Mater. Sci. Eng. 5 (4) (1970) 193–200, https://doi.org/10.1016/0025-5416(70)90081-9.

[76] Y. Estrin, H. Mecking, A unified phenomenological description of work hardening and creep based on one-parameter models, Acta Metall. 32 (1) (1984) 57–70, https://doi.org/10.1016/0001-6160(84)90202-5.

[77] J.G. Sevillano, No Title, in: H. Mughrabi (Ed.), Plast. Deform. Fract. Mater. Mater. Sci. Technol. Vol. 6, Weinheim, Germany, 1993: p. 19.

[78] R.F. Hehemann, Phase Transformation, in: Am. Soc. Met., Metals Park, Ohio, 1970: p. 397.

[79] M.-X. Zhang, P.M. Kelly, Determination of carbon content in bainitic ferrite and carbon distribution in austenite by using CBKLDP, Mater. Charact. 40 (3) (1998) 159–168, https://doi.org/10.1016/S1044-5803(98)00005-9.

[80] A. Ramazani, P.T. Pinard, S. Richter, A. Schwedt, U. Prahl, Characterisation of microstructure and modelling of flow behaviour of bainite-aided dual-phase steel, Comput. Mater. Sci. 80 (2013) 134–141, https://doi.org/10.1016/j.commatsci.2013.05.017.

[81] H.K.D.H. Bhadeshia, Bainite in Steels: Transformations, Microstructure and Properties, Second, IOM Communications Ltd, London, 2001. https://books.google.co.id/books?id=sF5RAAAAMAAJ.

[82] K. Zhu, O. Bouaziz, C. Oberbillig, M. Huang, An approach to define the effective lath size controlling yield strength of bainite, Mater. Sci. Eng. A. 527 (2010) 6614–6619, https://doi.org/10.1016/j.msea.2010.06.061.

[83] A. Ramazani, K. Mukherjee, A. Abdurakhmanov, U. Prahl, M. Schleser, Micro – macro-characterisation and modelling of mechanical properties of gas metal arc welded (GMAW), Mater. Sci. Eng. A 589 (2013) 1–14.

[84] G. Béres, Z. Weltsch, Estimation of strength properties from microhardness results in dual phase steels with different martensite volume fraction, Period. Polytech. Transp. Eng. (2018) 1–7, https://doi.org/10.3311/PPtr.12113.

[85] C. Thomser, Modelling of the mechanical properties of dual phase steels based on microstructure, Techn. Univ, Aachen, 2009.

[86] A. Ramazani, Y. Chang, U. Prahl, Characterization and modeling of failure initiation in bainite-aided DP steel, Adv. Eng. Mater. 16 (2014) 1370–1380, https://doi.org/10.1002/adem.201300556.

[87] T. Gladman, D. Dulieu, I. McIvor, Structure–Property Relationships in High Strength Microalloyed Steels, in: Microalloying 75, New York, 1977.

[88] C. Cayron, ARPGE: a computer program to automatically reconstruct the parent grains from electron backscatter diffraction data, J. Appl. Crystallogr. 40 (2007) 1183–1188, https://doi.org/10.1107/s0021889807048777.

[89] A. Anthoine, Derivation of the in-plane elastic characteristics of masonry through homogenization theory, Int. J. Solids Struct. 32 (1995) 137–163, https://doi.org/10.1016/0020-7683(94)00140-R.
[90] V.G. Kouznetsova, Computational homogenization for the multi-scale analysis of multi-phase materials, 2002. 10.6100/IR560009.
[91] F. Roters, D. Raabe, G. Gottstein, Work hardening in heterogeneous alloys - a microstructural approach based on three internal state variables, Acta Mater. 48 (2000) 4181–4189, https://doi.org/10.1016/S1359-6454(00)00289-5.
[92] C. Reuber, P. Eisenlohr, F. Roters, D. Raabe, Dislocation density distribution around an indent in single-crystalline nickel: comparing nonlocal crystal plasticity finite-element predictions with experiments, Acta Mater. 71 (2014) 333–348, https://doi.org/10.1016/j.actamat.2014.03.012.
[93] F. Roters, P. Eisenlohr, L. Hantcherli, D.D. Tjahjanto, T.R. Bieler, D. Raabe, Overview of constitutive laws, kinematics, homogenization and multiscale methods in crystal plasticity finite-element modeling: theory, experiments, applications, Acta Mater. 58 (2010) 1152–1211, https://doi.org/10.1016/j.actamat.2009.10.058.
[94] D. Peirce, R.J. Asaro, A. Needleman, An analysis of nonuniform and localized deformation in ductile single crystals, Acta Metall. 30 (1982) 1087–1119, https://doi.org/10.1016/0001-6160(82)90005-0.
[95] G. Voronoi, Nouvelles applications des paramètres continus à la théorie des formes quadratiques. Deuxième mémoire. Recherches sur les paralléllo̊edres primitifs, J. Für Die Reine Und Angew. Math. 134 (1908) 198–287. http://eudml.org/doc/149291.
[96] D. Q. Bai, A. Di Chiro, S. Yue, Stability of Retained Austenite in a Nb Microalloyed Mn-Si TRIP Steel, 1998. doi:10.4028/www.scientific.net/MSF.284-286.253.
[97] C. Garcia-Mateo, F.G. Caballero, J. Chao, C. Capdevila, C. Garcia De Andres, Mechanical stability of retained austenite during plastic deformation of super high strength carbide free bainitic steels, J. Mater. Sci. 44 (2009) 4617–4624, https://doi.org/10.1007/s10853-009-3704-4.
[98] C. García-Mateo, F.G. Caballero, The role of retained austenite on tensile properties of steels with bainitic microstructures, Mater. Trans. 46 (2005) 1839–1846, https://doi.org/10.2320/matertrans.46.1839.
[99] A.S. Podder, I. Lonardelli, A. Molinari, H.K.D.H. Bhadeshia, Thermal stability of retained austenite in bainitic steel: an in situ study, Proc. R. Soc. A Math. Phys. Eng. Sci. 467 (2011) 3141–3156, https://doi.org/10.1098/rspa.2011.0212.
[100] W. Österle, H. Rooch, A. Pyzalla, L. Wang, Investigation of white etching layers on rails by optical microscopy, electron microscopy, X-ray and synchroton X-ray diffraction, Mater. Sci. Eng. A. 303 (2001) 150–157, https://doi.org/10.1016/S0921-5093(00)01842-6.
[101] W. Lojkowski, M. Djahanbakhsh, G. Bürkle, S. Gierlotka, W. Zielinski, H.J. Fecht, Nanostructure formation on the surface of railway tracks, Mater. Sci. Eng. A. 303 (2001) 197–208, https://doi.org/10.1016/S0921-5093(00)01947-X.
[102] M. Steenbergen, R. Dollevoet, On the mechanism of squat formation on train rails - Part I: Origination, Int. J. Fatigue. 47 (2013) 361–372, https://doi.org/10.1016/j.ijfatigue.2012.04.023.
[103] W. Solano-Alvarez, E.J. Pickering, H.K.D.H. Bhadeshia, Degradation of nanostructured bainitic steel under rolling contact fatigue, Mater. Sci. Eng. A. 617 (2014) 156–164, https://doi.org/10.1016/j.msea.2014.08.071.